Volume 1 | Number 1 | Jan 2013 | Pages 1–100

Analyst

www.rsc.org/analyst

ROYAL SOCIETY OF CHEMISTRY

ROYAL SOCIETY OF CHEMISTRY

www.rsc.org/analyst

Selective detection of elemental mercury vapor using a surface acoustic wave (SAW) sensor

K. M. Mohibul Kabir[1], Ylias M. Sabri[1], Glenn I. Matthews[2], Lathe A. Jones[1], Samuel J. Ippolito[1,2*],

Suresh K. Bhargava[1*]

[1]Mercury Management and Chemical Sensing Laboratory (MMCSL), Centre for Advanced

Materials & Industrial Chemistry (CAMIC), School of Applied Sciences, RMIT University,

Melbourne, VIC 3001, Australia

[2]School of Electrical and Computer Engineering, RMIT University, Melbourne, VIC 3001,

Australia

E-mail: samuel.ippolito@rmit.edu.au, suresh.bhargava@rmit.edu.au

Phone: +61 3 9925 2330

Abstract. The detection of elemental mercury (Hg^0) within industrial processes is extremely important as it is the first major step in ensuring the efficient operation of implemented mercury removal technologies. In this study, a 131 MHz surface acoustic wave (SAW) delay line sensor with gold electrodes was tested towards Hg^0 vapor (24 to 365 ppb_v) with/without the presence of ammonia (NH_3) and humidity (H_2O), as well as volatile organic compounds (VOCs) such as acetaldehyde (MeCHO), ethylmercaptan (EM), dimethyl disulfide (DMDS) and methyl ethyl ketone (MEK), which are all common interfering gas species that co-exist in many industrial applications requiring mercury monitoring. The developed sensor exhibited a detection limit of 0.7 ppb_v and 4.85 ppb_v at 35 and 55°C, respectively. Furthermore, a repeatability of 97% and selectivity of 92% in the presence of contaminants gases was exhibited by the sensor at the chosen operating temperature of 55°C. The response magnitude of the developed SAW sensor towards different concentrations of Hg^0 vapor fitted well with the Langmuir extension isotherm (otherwise known as loading ratio correlation (LRC)) which is in agreement with our basic finite element method (FEM)

work where an LRC isotherm was observed for a simplified model of the SAW sensor responding to different Hg contents deposited on the Au based electrodes. Overall, the results indicate that the developed SAW sensor can be a potential solution for online selective detection of low concentrations of Hg^0 vapor found in industrial stack effluents.

1. Introduction

Anthropogenic mercury emission (i.e. from mining, combustion of fossil fuels and coal-fired power plants) is now considered a major global concern due to its detrimental effects on human health and the environment[1-3]. The total emission of gaseous mercury which originates from natural and anthropogenic sources in the form of elemental mercury (Hg^0) is estimated at 5500 tons per year[1-7]. Due to its high mobility and low vapor pressure Hg^0 vapor has the ability to travel long distances in the atmosphere as it can stay airborne for up to 5 years before it forms more toxic organic compounds[7-9]. Among these compounds, methyl mercury (CH_3Hg^+) in particular, can bio accumulate in seafoods and enter the food chain, thus severely affecting human health through kidney damage, neurotoxicity and causing cardiovascular diseases just to name a few[10-13]. Therefore the World Health Organization (WHO)[14] threshold exposure limit of Hg in the air is set at a low ~5.6 ppb_v. From anthropogenic point of view, reports indicate that mercury emissions have increased 3-4 times during the industrialization period[15-17]. Around 30% of these emissions have resulted from coal-fired power plants with release concentrations ranging from 0.1 to 2 ppb_v[18]. In order to limit anthropogenic mercury emissions, governments worldwide are introducing new and more stringent regulations[19]. For example, continuous detection of Hg emission in cement kilns in Germany has now become mandatory[20] with Hg emission limits being as low as ~6 and ~3.5 ppb_v for half-hourly and daily averages, respectively[21]. An important part of the mercury emission control process is mercury monitoring systems which provide feedback to the removal technology for efficient operation. It is therefore very important to develop a monitoring system at common emission sources for efficient measurement of Hg^0 vapor present among other contaminant gases.

Most of the commercially available mercury detection systems are based on atomic absorption spectroscopy (AAS) and atomic fluorescence spectrometry (AFS)[22, 23]. Although these techniques have been approved by United States Environmental Protection Agency (US-EPA) and possess high sensitivity towards Hg^0 vapor[24, 25], they tend to suffer from cross-sensitivity in the presence of common interfering gases such as NH_3, H_2O and volatile organic compounds (VOC), which results in inaccurate reporting of Hg^0 vapor concentration within many industrial applications. These methods can be aided with amalgamation techniques where the gas samples are separated and pre-concentrated using gold traps[26] to overcome the cross interference of the contaminant gases. However, the gold traps are required to be heated up-to $750°C$[27, 28] in order to release the trapped Hg^0 thereby making the operating lifetime and online monitoring capability of these methods very limited. In addition, these methods are associated with high cost, logistical and skilled personnel requirements which make these methods infeasible for real-world applications[29].

Alternative Hg^0 vapor detection methods based on micro-sensors employing either cantilever, acoustics, chemiresistive or surface plasmon resonance (SPR) techniques are primarily based on strong interaction between Hg^0 and Au (known as amalgamation) have also been investigated extensively[30-32]. More recently, researchers have employed Au nanostructures to increase the sensitivity of these types of sensors[14, 33]. However, the effect of common interferant gases on the sensitivity of these types of sensors still needs thorough study, as operation of these sensors in an industrial environment will always be in the presence of such impurities.

Our group has recently shown that mass-based Quartz Crystal Microbalance (QCM) sensors are highly selective towards Hg^0 vapor in the presence of interfering species such as NH_3, humidity and VOCs[29, 34]. However, the low sensitivity (limit of detection ~8 ppb_v at 35°C) of the QCM sensor limits the sensor from detecting low concentrations of Hg^0 vapor. Surface acoustic wave (SAW) sensors are an elite family of mass based micro-sensors[35, 36] which have the potential to possess much higher sensitivity towards Hg^0 vapor compared to a QCM based sensor[37]. SAW based sensors for detecting low concentrations of Hg^0 vapor was first demonstrated by Caron *et al.*[38], where they showed that a SAW delay line with aluminum interdigitated transducers (IDTs) and a thin film of

gold employed as sensing layer was capable of detecting low concentrations of Hg^0 vapor (down to 100 ppb_v) at different operating temperatures. A decade later Jasek *et al.*[39] presented a different SAW resonator design based on gold electrodes and reflector for detecting low concentrations (down to 300 ppb_v) of Hg^0 vapor. Recently, we have reported the cross sensitivity effect of common industrial relevant volatile organic compounds (VOCs) such as ethylmercaptan (EM), dimethyl disulphide (DMDS) and methyl ethyl ketone (MEK) on a SAW based Hg^0 vapor sensor[40]. However, the selectivity performance of the SAW based sensor towards Hg^0 vapor in critical conditions (dry and humid) as well as effect of other important interfering gas species such as ammonia (NH_3), acetaldehyde (MeCHO) etc. still need to be investigated and is necessary in determining the feasibility of the SAW based solid state sensor for efficient monitoring of Hg^0 vapor. Furthermore, the alteration of the SAW device designs to achieve better detection limit, repeatability and selectivity while measuring low concentrations of Hg^0 vapor, are yet to be investigated.

Typically, SAW transducers are used as mass-based sensors where mass perturbations on the sensing layer along the propagation path of the acoustic wave acts as the sensing mechanism[41]. The gas to be detected (analyte) interacts with a sensing film which is placed in between the input and output IDTs. This interaction results in a change in the acoustic wave velocity which is detected in the output IDT as a shift in the SAW resonant frequency (f_0). The shift in frequency is then related to the analyte concentration present in the atmosphere.

In this work, we demonstrate a two port SAW delay line sensor which employs the interdigitated transducers (IDTs) electrodes as the sole sensing element without introducing any additional sensing layer in-between the transmitting and receiving IDT. This approach in SAW based sensor design was found to be able to detect very low concentration of Hg^0 vapor in the presence of common interfering gases and humidity at the different operating temperatures tested. The interfering gases tested were NH_3, DMDS, MEK, EM and Acetaldehyde which are common gases present in industrial effluents.

2. Theoretical Modeling

In the current SAW sensor design, the resonant frequency of the sensor changes when Hg^0 vapor comes in contact with the Au electrode surface. The change in the resonant frequency of the sensor occurs due to the mechanical and acoustoelectric perturbations of the Au-thin film which results from Hg-Au amalgamation. The shift in resonant frequency due to Au-film mechanical perturbations can be represented by Equation 1[42] while the shift in SAW velocity results from the acoustoelectric perturbations can be expressed by Equation 2[43, 44].

$$\Delta f = (k_1 + k_2)f_0{}^2\rho h - k_2 f_0{}^2 \rho h \frac{4\mu}{v_0{}^2}\left(\frac{\lambda+\mu}{\lambda+2\mu}\right) \tag{1}$$

$$\frac{\Delta v}{v_0} = \frac{-k^2}{2}\frac{1}{1+\left(\frac{v_0\varepsilon\rho}{\sigma_{sh}}\right)^2} \tag{2}$$

In these equations, k_1 and k_2 represent substrate material's constant, ρ and h are Au film density and thickness, respectively, λ and μ are Au film's Lame constants, σ_{sh} is sheet conductivity of Au-film, ε_ρ is the effective permittivity of the structure including free space permittivity and k^2 represents the electro-mechanical coupling coefficient of the substrate material. From Equation 1, it can be observed that an increase in film density and thickness (related to mass loading) will result in a decrease in the resonant frequency of the sensor. On the other hand, an increase in the Lame constants (related to mechanical stiffness) will result in an increase in the resonant frequency. However, mechanical stiffening effect can be ignored for extremely thin films[42]. Therefore Equation 1 can be simplified in the form of Equation 3.

$$\Delta f = (k_1 + k_2)f_0{}^2\rho h \tag{3}$$

It can be observed from Equation 2 that the acoustoelectric response of the sensor is directly proportional to the electro-mechanical coupling coefficient of the device substrate material. This indicates that the SAW velocity shift due to acoustoelectric perturbations can be significant for SAW substrate with high electro-mechanical coefficient such as YZ $LiNbO_3$ (k^2=4.8). However,

this phenomenon is not as significant when ST- quartz is used as the SAW substrate due to its extremely low k^2 value (0.11).

The negative shifts in the resonant frequency (f_0) of the SAW sensor will be proportional to the concentration of Hg^0 vapor that comes in contact with the Au electrodes. As the number of Hg^0 monolayers formed on the Au surface is proportional to the Hg^0 vapor concentration, the resonant frequency shift will also be proportional to the number of Hg^0 monolayers formed on the Au surface. The higher the vapor concentration, the greater the number of Hg^0 monolayers that undergo sorption and diffusion; thus increasing the thickness and the effective mass density of the IDT electrode fingers.

In order to analyse the SAW device behaviour when Au electrodes are exposed to Hg^0 vapor, a series of finite element method (FEM) simulations were performed on a simplified SAW delay line model using a commercially available FEM package (COMSOL multiphysics 4.3b). As shown in Figure 1a, a simplified 2D SAW delay line structure with two pairs of gold electrodes (each having defined dimensions of 6 μm length and 100 nm thickness) in both the input and output IDTs placed on a quartz substrate was considered for simulation. The length and height of the simulated structure was 1000 and 500 μm, respectively. Full time-dependent analyses (60 ns simulation time) were performed in order to obtain the dynamic response of the simulated device. For all simulations, an impulse voltage (described by Equation 4) was applied to the input electrodes where V_+ and V_- was applied to the odd and even voltages, respectively.

$$V_+ = \begin{cases} 1V, 0 \leq t \leq 1ns \\ 0V, t \geq 1ns \end{cases} \qquad V_- = 0V \qquad\qquad (4)$$

The voltage of both even and odd output electrodes was set to zero and were coupled separately. The initial displacement fields both in the X and Y directions (U_x and U_y) along with initial structural velocity field $\partial U/\partial t$ were set to zero. FEM meshes for all simulations were arranged by keeping a density of 48 nodes per wavelength along the surface. Relatively coarser node density was maintained in the depth of the substrate. This was because the node density vertical axis was

not expected to affect the simulation result significantly given that the mismatch between the denser and coarser region was maintained in a minimum level throughout the depth. In addition, the coarser meshing in the depth of the structure was arranged to reduce the number of elements hence reducing the simulation time. However, the area immediately under the surface of the device was set to high node density of 24 per wavelength in order to obtain high accuracy of the results. As shown in Figure 1b, the meshing arrangement allowed for much higher node densities at the location of the surface, requiring a total of 36306 elements. Details of simulated SAW structure parameters are listed in Table 1 while material properties for quartz and unperturbed gold can be found elsewhere[45].

   A series of simulations were performed by varying the nominal number of Hg^0 monolayers formed on the Au electrodes between 1 and 50. The effective mass density per area and the thickness of the Au electrodes were varied according to the number of Hg^0 monolayers as shown in Table 1. These changes in effective mass density and the thickness of the Au electrodes for various number of Hg^0 monolayers were calculated based on reports that (i) each monolayer has a surface coverage[46] of 469 ng/cm^2, (ii) the Hg^0 atoms' diameter are 0.342 nm[47] and (iii) the Hg^0 atoms are diffused only up to top an Au depth of 10 nm from the surface[48]. For mercury coverage of 20 monolayers, it is assumed that both the effective mass density and the thickness of the Au electrodes are increased. At this coverage level, the process of diffusion and amalgamation is assumed to be significantly reduced[49] due to the Au surface reaching saturation thereby resulting in the effective mass density change approaching a maximum value (Table 1). Thereon, any additional mercury is assumed to be loosely adsorbed and contributes to increase in film thickness alone. After every simulation, the X component of the displacement field (defined as 'u' in COMSOL multiphysics) at the starting point (point 'P' in Figure 1a) of the output IDT was acquired. Figure 2a shows the X component of the displacement field at point 'P' at different times for both the unperturbed Au electrodes and Au electrodes containing 50 monolayers of Hg contents while the surface plots for total piezoelectric displacement under the IDT area when the simulations were performed with unperturbed Au electrodes and Au electrodes with 50 Hg^0 monolayers can be seen

from Figure 2c and 2d, respectively. As shown, the displacement field was delayed as the Hg^0 molecules were diffused into the Au electrodes. The time delay in displacement field can be directly related to the resonant frequency change of the SAW device. As stated in Table 2, the time delay in the displacement field varied between 0.0067 to 0.1845 ns for 1 to 50 Hg^0 monolayer formations on the Au electrodes. It was observed that the relationship between the time delay shifts over the number of monolayer formation followed the Langmuir extension isotherm (Figure 2b). This indicates that the SAW based Hg^0 vapor sensor with Au electrodes act as sensing elements can be well suited for detection of low concentrations of Hg^0 vapor since higher dynamic response can be obtained between relatively lower concentrations of Hg^0 vapor.

3. Experimental

3.1 SAW fabrication & oscillator setup

A SAW delay line device with two ports was fabricated on a ST-X cut quartz substrate (Figure 3). ST-X cut quartz (which is also referred as 42.75° rotated Y cut Quartz) was chosen for its relatively better temperature stability at 20-60°C than other common substrate cuts used for SAW device fabrication (such as XY Lithium Niobate or 36°YX Lithium Tantalate)[50]. Initially, a 20 nm thick Titanium (Ti) and a 30 nm thick Nickel (Ni) adhesion layer followed by a 50 nm thick Au layer was evaporated on a 15 mm×9 mm quartz substrate. Standard photolithography processes were used to pattern the input and output IDT electrode fingers. Both the input and output IDTs were patterned with 180 finger pairs with all electrode fingers having a width and spacing of 6 µm, which resulted in acoustic wavelength (λ) of 24 µm. The aperture width (w) was 1700 µm for all electrodes and the delay line length was kept at 75λ as shown in Figure 3. Using a Rhode & Schwartz vector network analyzer, the scattering parameters of the fabricated sensor was tested. An insertion loss of -11 dB was observed at the center frequency of approximately 131 MHz.

A radio frequency (RF) amplifier was designed and fabricated to be used to construct the SAW oscillator circuit by connecting it on a feedback path of the SAW sensor. The fabricated amplifier was measured to have 27 to 29 dB gain at 100MHz to 300MHz frequency which made it suitable for the SAW device fabricated.

3.2 Hg^0 vapor testing

The fabricated sensor was placed securely inside a test cell having a volume of ~100 ml. A PID temperature controller was used to generate different concentrations of Hg^0 vapor by changing the temperature of a Hg^0 permeation tube (VICI, TX, USA). The target rate of the permeation tube was 3100 ng/min at 100°C (as certified by NIST). A temperature range of 40°C to 80°C was set on the mercury generator to produce the different concentrations of Hg^0 vapor tested. The permeation rate (i.e. Hg^0 vapor concentration generated) was re-confirmed by taking a series of wet chemical trapping experiments based on a modified version of the Ontario Hydro method by capturing the generated Hg^0 vapor in a train of four potassium permanganate (KMnO$_4$) trapping solutions at the point before the vapor entered the sensor cell and analyzing the taped solution for mercury by Inductively coupled plasma mass spectrometry (ICP-MS). The temperature of the sensor cell was controlled by thermocouples providing feedback to the heater. A multi-channel mass flow controller (MFC) system was used to control the flow of Hg^0 vapor, H$_2$O vapor and of the five different interfering gases tested which were stored in five different cylinders. A constant total flow of 200 standard cubic centimeters (sccm) in the sensor cell was maintained throughout the whole experiment. The oscillation frequency of the SAW device was continuously monitored with an Agilent 53131A frequency counter. A block diagram of the experimental setup used can be found in the supplementary information, SI, Figure S1.

The sensing performance of the developed sensor was tested by exposing it towards Hg^0 vapor concentrations of 24, 51, 104, 142, 195, 265 and 365 ppb$_v$. Each mercury pulse consisted of a 30 minute Hg^0 vapor exposure followed by a 90 minute dry N$_2$ purge in order to allow the sensor to return to its center frequency through the desorption of Hg^0 from the gold electrode surfaces. It should be noted that desorption process used to regenerate the sensor surface between each pulse was accomplished by only switching the stream to dry N$_2$ gas flow without changing the operating temperature or the total flow rate. This sequence is referred to as a pulse throughout the remainder of the manuscript. The selectivity tests involved exposing the SAW based sensor towards different concentrations of Hg^0 vapor in the presence of 383.8 ppm$_v$ ammonia (NH$_3$), 303.4 ppm$_v$

acetaldehyde (MeCHO), 2.61 ppm_v ethylmercaptan (EM), 5.01ppm_v dimethyl disulfide (DMDS),

40.1 ppm_v methyl ethyl ketone (MEK) and H_2O vapor (with equivalent relative humidity (RH) of 50

and 20% at 35 and 55°C, respectively).

The noise profiles of the sensor following Hg^0 exposure tests at different operating temperatures

between 35 and 75°C (with 10°C increments) were recorded for a period of 1 hour while flushing

the sensor chamber with dry nitrogen (N_2). The noise profiles were used later to calculate the limit

of detection (LOD) of the developed SAW sensor at different operating temperatures. Noise profiles

of the sensor for different operating temperatures are shown in SI, Figure S2. It can be observed that

the sensor exhibited higher noise magnitudes at elevated operating temperatures. This is primarily

thought to result from the temperature fluctuations (±0.3°C) of the temperature controller that was

used in this study. The sensor showed almost similar noise magnitudes while operating at 35 to

55°C while higher noise magnitudes were observed beyond 55°C. This can be explained since the

temperature coefficient of ST cut quartz has higher sensitivity to temperature fluctuations when

operated at higher temperatures[50].

4. Results and Discussion

4.1 Sensor performance at different operating temperatures

The sensor was tested towards different concentrations of Hg^0 vapor ranging from 24 to 365 ppb

at operating temperatures between 35 and 75°C in 10°C increments. Each exposure to mercury

vapor resulted in the oscillation frequency reducing as a function of both exposed Hg^0 vapor

concentration as well as the operating temperature. An example of the sensors dynamic response

towards the different concentrations of Hg^0 vapor at 55°C can be seen from Figure 4a. As shown,

during the Hg^0 vapor exposure period (30 minutes) of every pulse, the sensor response exhibited a

negative shift in operating frequency. Upon exposure, the Hg^0 vapor atoms are expected to deposit

on the Au electrode surface due to the high affinity between the two metals that result in the

formation of Hg-Au amalgams. This process results in the mechanical and acoustoelectric

perturbations of the Au electrodes thereby resulting in sensor's oscillation frequency to change according to Equation 2 and 3, as described in Section 2.

As can be observed from Figure 4a, the desorption process was started well before the sensors response magnitude reached the saturation yet it operated well as a sensor towards different concentrations of Hg^0 vapor. This 30 minutes exposure time was based on our previous observations where it was found that the Au based transducer can take up-to 8 hours before reaching the saturation, a period that is not suitable for industrial use where fast turn-around times are required[29, 40]. Interestingly, no external heat and change in flow rate during the regeneration period was required for the developed sensor.

The response magnitude of the developed sensor towards the different Hg^0 vapor concentrations tested was used to obtain the calibration curve at each operating temperature. It was observed that the sensor response magnitude was related to the Hg^0 vapor concentration (calibration curve) through the Langmuir extension isotherm or LRC (Equation 5) at all the operating temperatures tested (Figure 4b shows LRC for 55°C). LRC for other tested operating temperatures are shown in SI, Figure S3.

$$\Delta f = \frac{ab[Hg]^c}{(1+b[Hg]^c)} \ . \tag{5}$$

In Equation 5, Δf represents the SAW response magnitude, $[Hg]$ represents Hg^0 vapor concentrations exposed to the sensor while a, b and c are constants.

These experimental observations are in line with the FEM modeling findings where the sensor response (time delay) was found to follow the same trend (LRC) against the number of Hg^0 monolayers formed on the Au surface, which is proportional to the Hg^0 vapor concentration in the atmosphere. The sensitivity of the developed SAW sensor towards Hg^0 vapor is deduced to be dependent on the concentration being measured, the relation of which can be derived from the derivative of the calibration curve (Equation 5) as presented in Equation 6. It can be deduced that the sensitivity decreases with increasing Hg^0 vapor concentration, indicating that the developed

sensor is designed well to detect low concentrations of Hg^0 vapor usually present in industrial stack effluents.

$$sensitivity = \frac{df}{d[Hg]} = \frac{abc[Hg]^{c-1}}{(1+b[Hg]^c)^2} \quad . \tag{6}$$

In order to determine the optimum operating temperature for the developed SAW based Hg^0 vapor sensor, the temperature profile of the sensor was acquired (Figure 5a) and critically analysed. The temperature profile of the sensor was obtained by exposing it towards Hg^0 vapor pulses in order of low to high concentrations at different operating temperatures. From the response magnitude perspective, it can be observed that the sensor exhibited the highest response magnitudes towards Hg^0 vapor when operated at 35°C. It can also be seen that, for elevated operating temperatures (45 to 75°C) the response magnitudes of the sensor did not vary significantly. Furthermore, the limit of detection (LOD) was also favorable at 35°C relative to all other operating temperatures tested. In order to determine the LOD of the sensor towards Hg^0 vapor, the method of three standard deviations was employed to the noise profile of the Hg exposed sensor. This data was acquired by exposing the sensor towards dry N_2 for one hour period at all operating temperatures (as discussed in section 3.2). The LOD of the sensor at different operating temperatures was observed to increase with increasing operating temperature and range between 0.7 ppb_v and ~15ppb_v as seen in Figure 5b. This trend can be explained by the noise magnitudes of the sensor which were also found to increase with increasing operating temperature. However, due to the similar noise magnitudes and sensitivity, the LOD of the sensor was found to be almost identical (4.50 ppb_v and 4.54 ppb_v) at 45 and 55°C, respectively. However from the operability perspective the higher temperature of 55°C is favored over 45°C as the effect of cross-contamination from interfering gas species has been reported to reduce with increasing operating temperature when detecting mercury with mass-based sensors. Therefore the operating temperatures of 35 and 55°C were chosen for further tests as the sensor has the lowest detection limit at 35°C while expected to have better selectivity towards low concentrations of Hg^0 vapor at 55°C.

4.2 Repeatability and stability of the SAW based Hg^0 vapor sensor

The repeatability of the developed sensor was tested by comparing the response magnitude of the sensor towards a series of six Hg^0 vapor pulses having the same concentration (365 ppb_v). In order to compare the repeatability of the developed SAW sensor at two different operating temperatures (35 and 55°C), the coefficient of variances (COV) was calculated for the sensor response magnitudes in the series at both temperatures. The COV is a measurement of the spread of a dataset around its mean and is therefore a good indication of the sensor repeatability[51]. A lower value of COV is an indication of better repeatability of the sensor (i.e. repeatability = 100% - COV). The mean or average response magnitude ($\Delta f_{Hg(avg.)}$) and standard deviation (σ) of the sensor response can be calculated using Equation 7 and Equation 8, respectively.

$$\Delta f_{Hg(avg.)} = \frac{\Sigma \Delta f_{Hg}}{n} \qquad (7)$$

$$\sigma = \sqrt{\frac{\Sigma (\Delta f_{Hg} - \Delta_{Hg(avg.)})^2}{n-1}} \qquad (8)$$

The symbol Δf_{Hg} represents the sensor's response magnitude for each Hg^0 vapor pulse, $\Delta f_{Hg(avg.)}$ is the average response magnitude of the repeated Hg^0 vapor pulses and n is the total number of Hg^0 vapor pulses. It was found that the sensor's response magnitude for the six repeated pulses varied by around ~3% (otherwise referred to as 97% repeatability) while measuring 365 ppb_v of Hg^0 vapor at 35 and 55°C (as shown in Figure 6a, 6b), indicating that the developed sensor had excellent repeatability at both operating temperatures tested.

From a long-term sensor stability point of view, we have previously reported that mass based acoustic wave sensors can efficiently detect Hg^0 vapor for up-to a six months period[29] while still being operable. In this study, it can be observed from SI, Figure S4 that the developed sensor's response magnitude towards a Hg^0 vapor concentration of 195 ppb_v only deviated by less than 5% following a testing period of one week. Furthermore, the SAW transducer was observed to oscillate and operate as a sensor following four weeks of experimental testing.

4.3 Selectivity of SAW towards Hg^0 vapor sensor

The selectivity of the developed SAW sensor towards Hg^0 vapor was tested by exposing the sensor towards Hg^0 vapor of different concentrations in the presence of common interfering gas species present in industrial environments. The concentrations used for different interfering gases are listed in Section 3.2. The concentrations of the common interference gas species used in this study are much higher than their normal levels in an industrial environment (low ppb_v levels)[52]. The higher concentrations were chosen for testing in order to realize the developed sensor's cross-sensitivity performance when operated under extreme environmental conditions.

Example of selectivity test for Hg^0 vapor concentrations of 365 ppb_v at an operating temperature of 55°C is shown in Figures 7a. As labeled in the figure, the tests involved exposing the sensor to clean Hg^0 vapor pulses while one or more interfering gases (NH_3, MeCHO, EM, DMDS, MEK and H_2O vapor) are added with the Hg^0 vapor in each alternative pulse. The selectivity of the developed SAW based Hg^0 vapor sensor for different interfering gases was calculated using Equation 9.

$$\boldsymbol{Selectivity}\,(\%) = \left(\mathbf{1} - \frac{\left| \Delta f_{(Hg^0)} - \Delta f_{(Hg^0+int.gas)} \right|}{\Delta f_{(Hg^0)}} \right) \times \mathbf{100}\% \qquad . \qquad (9)$$

The symbols $\Delta\boldsymbol{f}_{(Hg^0+int.gas)}$ and $\Delta\boldsymbol{f}_{(Hg^0)}$ represent the sensor's response magnitude towards Hg^0 vapor with and without the presence of interfering gases, respectively.

The sensor showed excellent selectivity at both operating temperatures of 35°C (89 to 92%) and 55°C (93 to 97%) when the tests were performed under dry conditions (i.e. without the presence of humidity). The overall selectivity data is shown in Figure 7b and tabulated in Table 3. It can be observed that the sensor exhibited better selectivity for all tested interfering gases when the operating temperature was increased from 35 to 55°C. Moreover the sensor showed much higher response (spikes of several kHz) towards Hg^0 vapor when in the presence of a humidity level of 20.6 g/m³ (equivalent 50% RH at 35°C) at the operating temperature of 35°C. As shown in Figure S5a, the sensor showed almost double the response magnitudes when humidity was introduced with 365 ppb_v of Hg^0 vapor at 35°C compared to Hg^0 vapor exposure alone. Therefore, it can be assumed that the sensor had no selectivity ($\Delta f_{(Hg^0+int.gas)}$ set to 0 Hz by default) towards

Hg^0 vapor in the presence of humidity at 35°C. However, the sensor showed excellent selectivity when the same humidity concentration (20.6 g/m^3 = 20% RH at 55°C) was present at 55°C (Figure S5b). As shown in Figure 7b and Table 3, the developed sensor showed selectivity of 92 to 96% for Hg^0 vapor exposure along with different interfering gases while in the presence of H_2O vapor. This observation is in agreement with past studies which have shown that mass based Hg^0 vapor sensors (i.e. QCMs) exhibit better selectivity at relatively higher operating temperatures[29]. It is postulated that the sensor stopped functioning at the lower tested operating temperature of 35°C in humid conditions due to the dew point (23°C) being close to the operating temperature. This has likely resulted in water molecules condensing on the IDTs which resulted in meaningless and abrupt frequency changes in the sensor response profiles thus it was not possible for the developed SAW sensor to detect Hg^0 vapor in the presence of such high humidity content at 35°C. The higher selectivity of the sensor observed at the elevated operating temperature is postulated to be due to the relatively higher vapor pressure of H_2O at 55°C and the fact that this temperature is relatively much higher than the dew point (23°C) thus ensuring that most of the H_2O molecules are in the gaseous form and do not condense onto the sensor surface.

5. Conclusions

In summary, a SAW sensor employing gold IDTs as the sensing elements was developed and tested for selective detection of low concentrations of Hg^0 vapor of low ppb$_v$ levels in the presence of NH_3, VOCs and high humidity content at both 35 and 55°C. The response magnitude of the developed SAW sensor towards different concentrations of Hg^0 vapor fitted well with the LRC which was in line with our theoretical FEM modeling. The LRC model fit further confirmed that the sensor design is well suited for detecting low concentration of Hg^0 vapor. It was also found that there is a tradeoff in the operating conditions to be chosen such that although the sensitivity of the developed SAW sensor decreases with increasing temperature, the selectivity towards Hg^0 vapor increases. The operating temperature at which the sensor was found to simultaneously have excellent sensitivity, repeatability and selectivity towards Hg^0 vapor among common interfering

gases both in dry and humid conditions was found to be 55°C. Moreover, these sensitivity, repeatability and selectivity was observed without the Au based SAW sensor requiring any external heat source or change in total flow rate during the regeneration step. The promising results make this sensor a potential solution for detecting low concentration of Hg^0 vapor in industrial stack effluents where the presence of interfering gases and humidity is very common.

1
2
3
4
5
6
7
8
9
10
11
12
13
14
15
16
17
18
19
20
21
22
23
24
25
26
27
28
29
30
31
32
33
34
35
36
37
38
39
40
41
42
43
44
45
46
47
48
49
50
51
52
53
54
55
56
57
58
59
60

References

1.   US-EPA, *Mercury Study Report to Congress, Volume I*, United States Environmental Protection Agency, 1997.

2.   US-EPA, *Mercury Study Report to Congress, Volume II*, United States Environmental Protection Agency, 1997.

3.   US-EPA, *Mercury Study Report to Congress, Volume III*, United States Environmental Protection Agency, 1997.

4.   N. Pirrone, S. Cinnirella, X. Feng, R. Finkelman, H. Friedli, J. Leaner, R. Mason, A. Mukherjee, G. Stracher and D. Streets, *Atmos. Chem. Phys.*, 2010, **10**, 5951-5964.

5.   E. G. Pacyna, J. M. Pacyna, F. Steenhuisen and S. Wilson, *Atmos. Environ.*, 2006, **40**, 4048-4063.

6.   J. Pacyna and J. Münch, *Water Air & Soil Pollution*, 1991, **56**, 51-61.

7.   UNEP, *Global Mercury Assessment 2013: Sources, Emissions, Releases and Environmental Transport*, UNEP Chemicals Branch, Geneva, Switzerland, 2013.

8.   D. W. Boening, *Chemosphere*, 2000, **40**, 1335-1351.

9.   W. H. Schroeder and J. Munthe, *Atmos. Environ.*, 1998, **32**, 809-822.

10.   D. M. Riley, C. A. Newby, T. O. Leal-Almeraz and V. M. Thomas, *Environ. Health Perspect.*, 2001, **109**, 779.

11.   P. W. Davidson, G. J. Myers and B. Weiss, *Pediatrics*, 2004, **113**, 1023-1029.

12.   K. B. Carman, E. Tutkun, H. Yilmaz, C. Dilber, T. Dalkiran, B. Cakir, D. Arslantas, Y. Cesaretli and S. A. Aykanat, *European journal of pediatrics*, 2013, **172**, 821-827.

13.   T. Syversen and P. Kaur, *J. Trace Elem. Med. Biol.*, 2012, **26**, 215-226.

14.   T. P. McNicholas, K. Zhao, C. Yang, S. C. Hernandez, A. Mulchandani, N. V. Myung and M. A. Deshusses, *J. Phys. Chem. C*, 2011, **115**, 13927-13931.

15.   L. D. Hylander and M. Meili, *Sci. Total Environ.*, 2003, **304**, 13-27.

16.   T. W. Clarkson, *Critical reviews in clinical laboratory sciences*, 1997, **34**, 369-403.

17.   K. R. Mahaffey, *Transactions of the American Clinical and Climatological Association*, 2005, **116**, 127.

18.   C. L. Senior, A. F. Sarofim, T. Zeng, J. J. Helble and R. Mamani-Paco, *Fuel Process. Technol.*, 2000, **63**, 197-213.

19.   J. Qiu, *Nature*, 2013, **493**, 144-145.

20.   R. Renzoni, C. Ullrich, S. Belboom and A. German, *Université de Liège. Independently commissioned by CEMBUREAU-CSI*, 2010.

21.   S. J. Ippolito, Y. M. Sabri and S. K. Bhargava, in *Environmental Chemistry and Toxicology of Mercury*, 2012, p. 59.

22.   P. D. Selid, H. Xu, E. M. Collins, M. Striped Face-Collins and J. X. Zhao, *Sensors*, 2009, **9**, 5446-5459.

23.   T. Anderson, J. Magnuson and R. Lucht, *Appl. Phys. B: Lasers Opt.*, 2007, **87**, 341-353.

24.   N. Bansal, J. Vaughan, A. Boullemant and T. Leong, 2013.

25.   D. L. Laudal, J. S. Thompson, J. H. Pavlish, L. A. Brickett and P. Chu, *Fuel Process. Technol.*, 2004, **85**, 501-511.

26.   G. Sällsten and K. Nolkrantz, *Analyst*, 1998, **123**, 665-668.

27.   M. G. Schweyer, J. C. Andle, D. J. McAllister and J. F. Vetelino, *Sens. Actuators, B*, 1996, **35**, 170-175.

28.   M. V. Balarama Krishna, D. Karunasagar, S. V. Rao and J. Arunachalam, *Talanta*, 2005, **68**, 329-335.

29.   Y. M. Sabri, S. J. Ippolito, J. Tardio, V. Bansal, A. P. O'Mullane and S. K. Bhargava, *Sci. Rep.*, 2014, **4**, 6741.

30.   T. Morris and G. Szulczewski, *Langmuir*, 2002, **18**, 5823-5829.

31.   X. Lou, G. Somesfalean, S. Svanberg, Z. Zhang and S. Wu, *Optics express*, 2012, **20**, 4927-4938.

32.   B. Rogers, L. Manning, M. Jones, T. Sulchek, K. Murray, B. Beneschott, J. Adams, Z. Hu, T. Thundat and H. Cavazos, *Rev. Sci. Instrum.*, 2003, **74**, 4899-4901.

33.   J. Z. James, D. Lucas and C. P. Koshland, *Environ. Sci. Technol.*, 2012, **46**, 9557-9562.

34.   Y. M. Sabri, A. Esmaielzadeh Kandjani, S. J. Ippolito and S. K. Bhargava, *ACS Appl. Mater. Interfaces*, 2015, **7**, 1491-1499.

35.   F. Bender, R. E. Mohler, A. J. Ricco and F. Josse, *Anal. Chem.*, 2014, **86**, 11464-11471.

36.   C.-L. Hsu, C.-Y. Shen, R.-T. Tsai and M.-Y. Su, *Sensors*, 2009, **9**, 980-994.

37.   K. M. Kabir, S. J. Ippolito, Y. M. Sabri, C. J. Harrison, G. Matthews and S. K. Bhargava, 2014.

38.   J. J. Caron, R. B. Haskell, P. Benoit and J. F. Vetelino, *IEEE Transactions on Ultrasonics, Ferroelectrics, and Frequency Control*, 1998, **45**, 1393-1398.

39.   K. Jasek, S. Neffe and M. Pasternak, *Acta Phys. Pol., A*, 2012, **122**, 825.

40.   K. M. Kabir, Y. M. Sabri, G. I. Matthews, S. J. Ippolito and S. K. Bhargava, *Sens. Actuators, B*, 2015, **212**, 235-241.

41.   W. P. Jakubik, *Thin Solid Films, Elesevier*, 2011.

42.   H. Wohltjen, *Sensors and Actuators*, 1984, **5**, 307-325.

43.   D. Ballantine Jr, R. M. White, S. J. Martin, A. J. Ricco, E. Zellers, G. Frye and H. Wohltjen, *Acoustic Wave Sensors: Theory, Design, & Physico-Chemical Applications*, Academic press, 1996.

44.   A. Ricco, S. Martin and T. Zipperian, *Sensors and Actuators*, 1985, **8**, 319-333.

45. B. A. Auld, *Acoustic fields and waves in solids*, John Wiley, 1973.

46. T. Morris, J. Sun and G. Szulczewski, *Anal. Chim. Acta*, 2003, **496**, 279-287.

47. R. B. Haskell, The University of Maine, 2003.

48. M. Fialkowski, P. Grzeszczak, R. Nowakowski and R. Holyst, *J. Phys. Chem. B*, 2004, **108**, 5026-5030.

49. M. Levlin, E. Ikavalko and T. Laitinen, *Fresenius. J. Anal. Chem.*, 1999, **365**, 577-586.

50. J. J. Caron, J. Andle and J. F. Vetelino, 1996.

51. G. F. Reed, F. Lynn and B. D. Meade, *Clin. Diagn. Lab. Immun.*, 2002, **9**, 1235-1239.

52. K. Na, Y. P. Kim, K.-C. Moon, I. Moon and K. Fung, *Atmos. Environ.*, 2001, **35**, 2747-2756.

Figure Captions

Figure 1. a) Simulated SAW delay line structures with 2 pairs of gold electrodes at both of the input and output IDTs placed on a quartz substrate. **b)** FEM mesh used for all simulations.

Figure 2. a) Time delay between the X displacement for the SAW structure simulated with a clean Au electrode and with an Au electrode having 50 monolayers of Hg^0 atoms. **b)** Langmuir curve fit for time delay in the displacement field against different number of monolayers formed on the Au electrodes. **c)** Surface plot showing the total piezoelectric displacement under the IDT area of the SAW structure for unperturbed Au electrodes and **d)** Au electrodes with 50 Hg^0 monolayers.

Figure 3. Image of the fabricated SAW sensor utilizing a ST quartz substrate and gold IDTs

Figure 4. a) Sensor's dynamic response for the different Hg^0 vapor concentrations tested at 55°C. **b)** Demonstration of Langmuir adsorption isotherm fitting on the sensor calibration curve at 55°C.

Figure 5. a) Sensor's temperature profile showing temperature dependency of the sensor for different concentrations of Hg^0 vapor. **b)** Detection limit of the sensor at different operating temperatures.

Figure 6. a) Example of sensor repeatability showing dynamic responses for six repeated pulses of 365 ppb_v Hg^0 vapor at 55°C and **b)** Repeatability (indicated by 100%-COV) of the sensor for six repeated pulses of 365 ppb_v Hg^0 vapor at 55 and 35°C. The dashed line (along 100% normalized response magnitude) indicates the average response magnitude of the sensor for the repeated pulses. Normalized response magnitude is calculated as the ratio of (in %) response magnitude to that of average response magnitude over six pulses ($\Delta f / \Delta f_{avg} \times 100\%$).

Figure 7. a) Sensor dynamic response for different interfering gases exposed with 365 ppb_v of Hg^0 vapor at operating temperature of 55°C and **b)** Bar graph shows overall selectivity of the sensor Hg^0 vapor exposure in the presence of various interfering gases while operating at 35 and 55°C.

Table Captions

Table 1. Parameters of simulated SAW delay line structure

Table 2. The time delay calculated from FEM simulation obtained for different numbers of monolayers adsorbed/diffused on the Au electrode

Table 3. Selectivity of the sensor towards 365 ppb_v Hg^0 vapor in the presence of different interfering gases
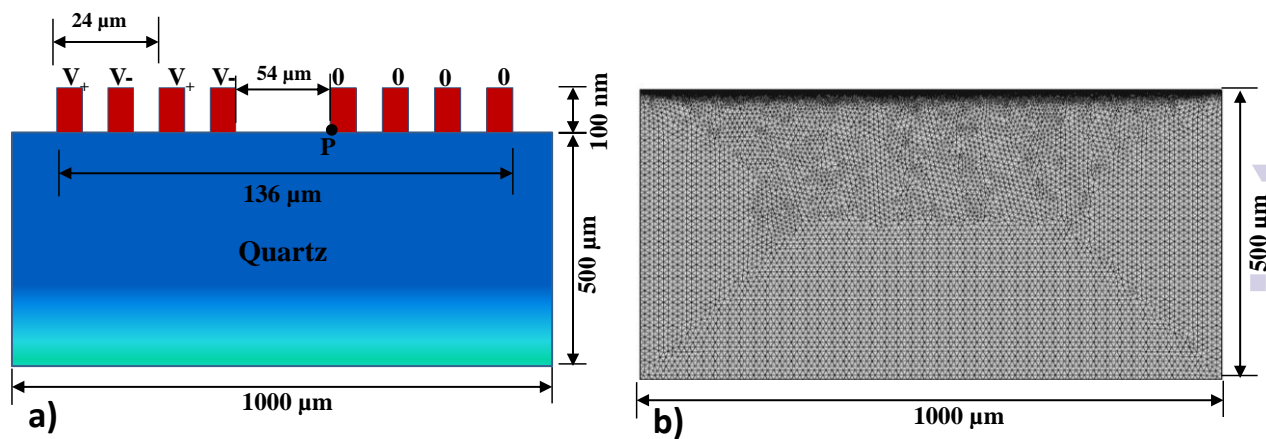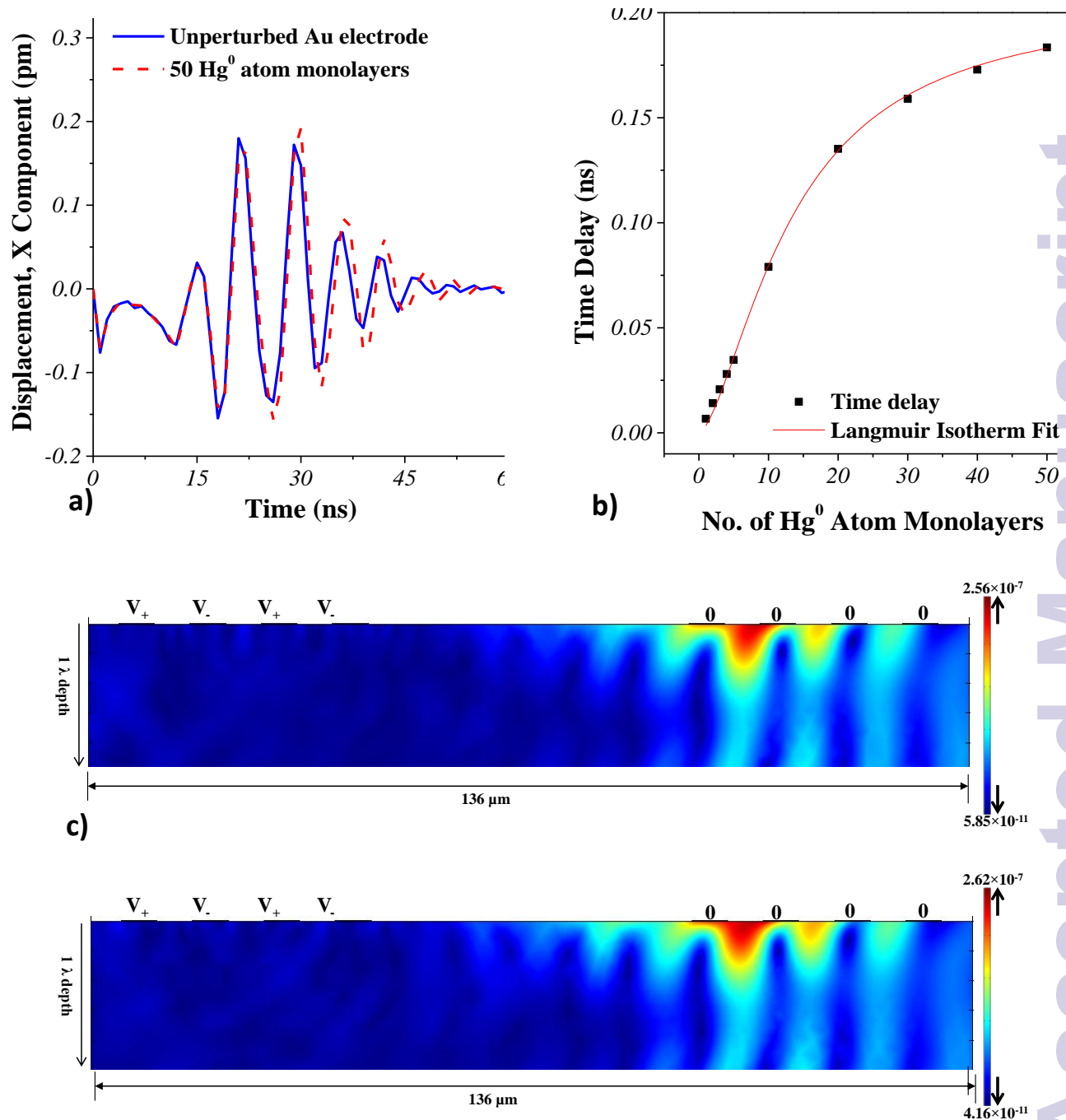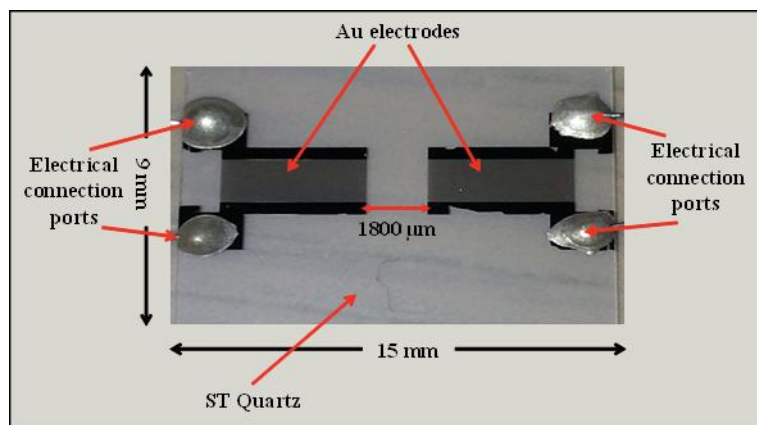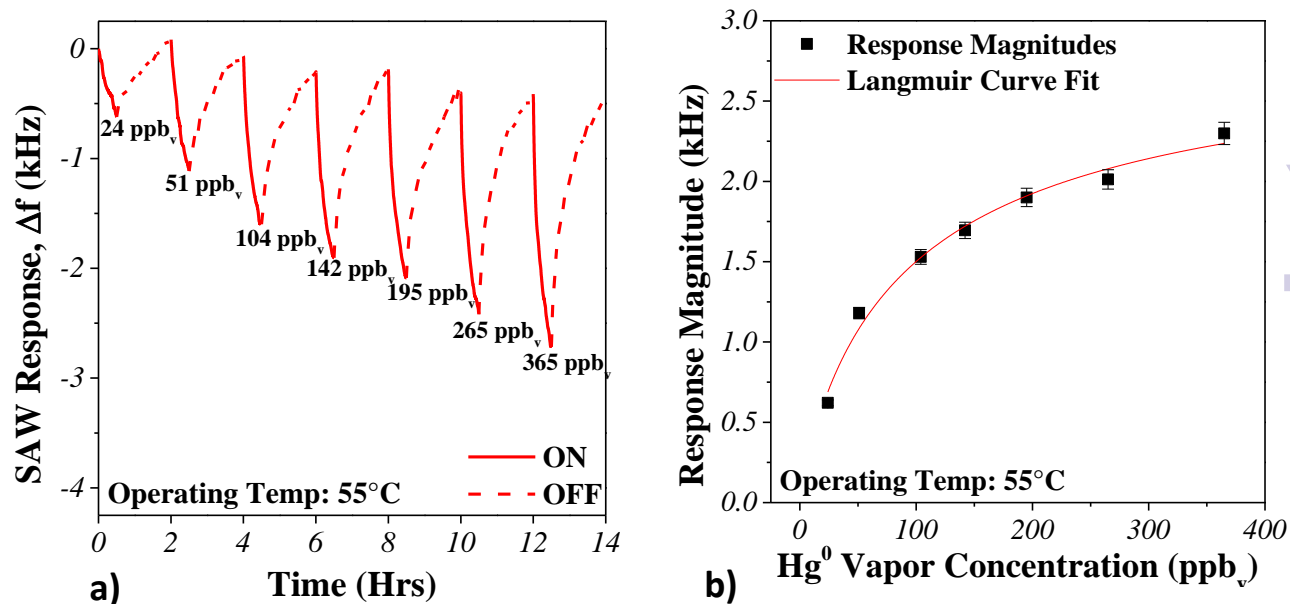
Figure 1

Figure 2

Figure 3

Figure 4

a)

b)

Figure 5

Figure 6

A= 383.8 ppm$_v$ NH$_3$ B= 303.4 ppm$_v$ MeCHO   C= 2.61 ppm$_v$ EM
D= 5.01 ppm$_v$ DMDS   E= 40.1 ppm$_v$ MEK   F= 20.6 g/m^3 H$_2$O
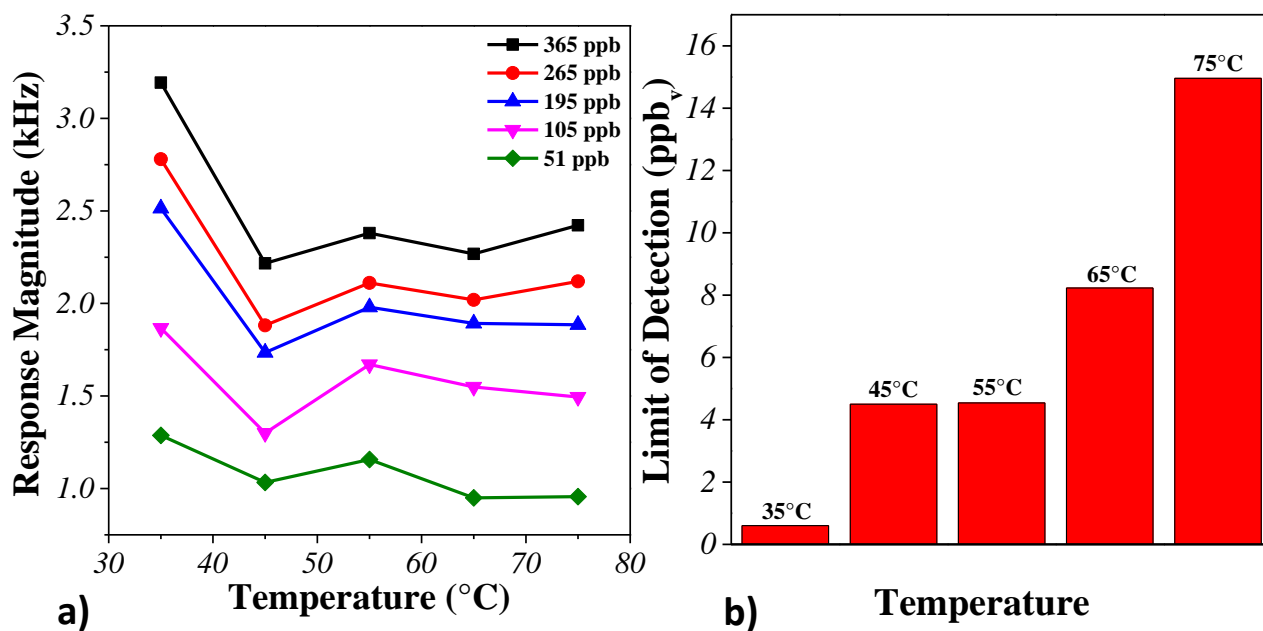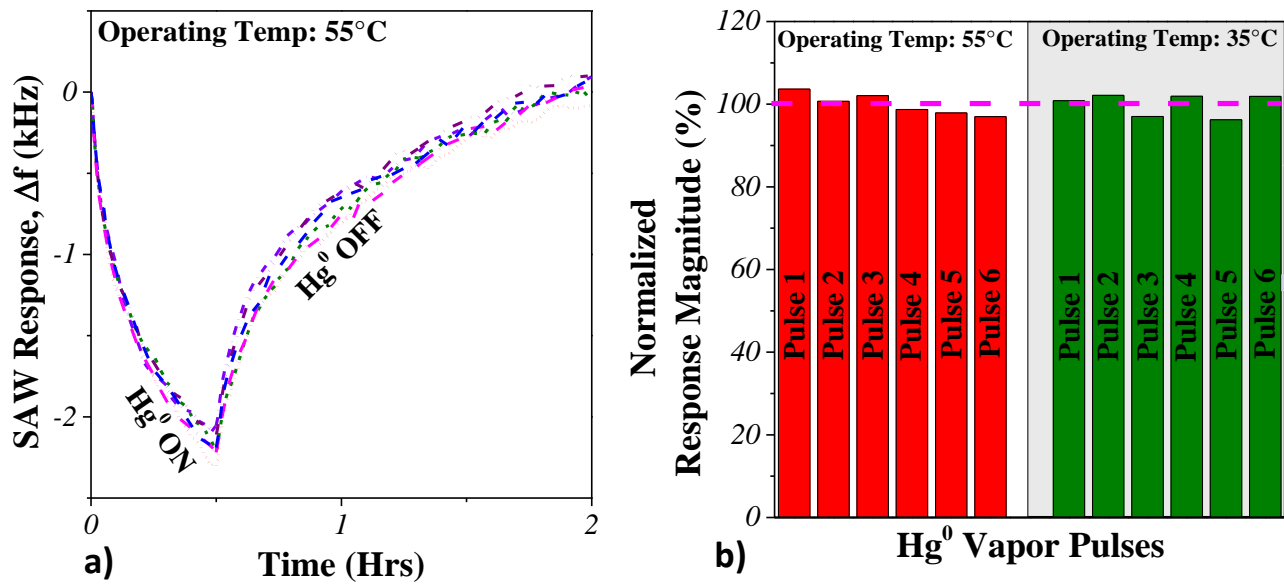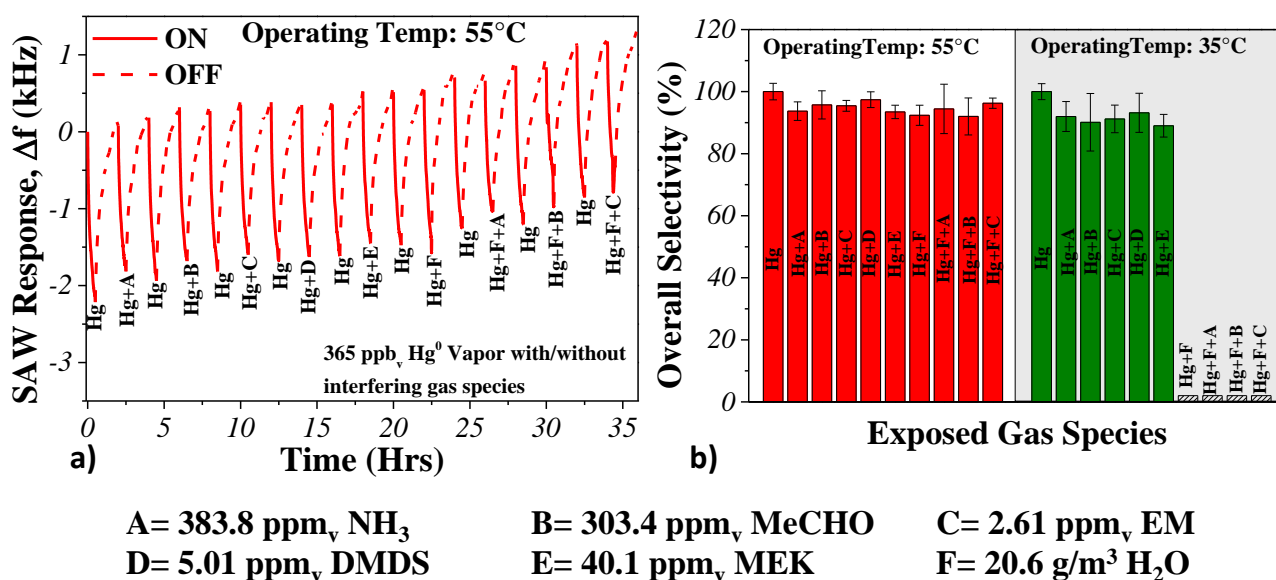
Figure 7

Table 1

SAW structure parameter	Value
Substrate Length	1000 µm
Substrate Height	500 µm
No. of Electrode pairs	2 (in both IDTs)
Electrode Length	6 µm
Electrode Height	100 nm
Wavelength	24 µm
Delay line length	54 µm

Table 2

No. of Hg^0 Monolayers	Effective Au mass density (g/cm^3)	Effective Au Electrode Thickness (μm)	Time Delay (ns)
1	19.77	0.100342	0.0067
2	20.24	0.100684	0.0141
3	20.71	0.101026	0.0207
4	21.18	0.101368	0.028
5	21.65	0.101710	0.0347
10	23.99	0.103420	0.0708
20	28.68	0.106840	0.1452
30	28.68	0.110260	0.1579
40	28.68	0.113680	0.1709
50	28.68	0.117100	0.1845

Table 3

Tested interfering gases along with Hg^0 vapor	Hg^0 Vapor Selectivity (%)	
	55°C	**35°C**
NH_3	93.7	91.9
MeCHO	95.7	90.1
EM	95.4	91.2
DMDS	97.4	93.2
MEK	93.5	89.0
H_2O Vapor	92.4	0
H_2O Vapor and NH_3	94.4	0
H_2O Vapor and CH_3CHO	92.0	0
H_2O Vapor and EM	96.3	0